

The VISCACHA survey – IX. The SMC Southern Bridge in 8D

M. C. Parisi¹,^{1,2}★ R. A. P. Oliveira¹,^{3,4}★ M. S. Angelo,⁵★ B. Dias¹,⁶★ F. F. S. Maia¹,⁷
 S. Saroon,⁶ C. Feinstein,^{8,9} J. F. C. Santos, Jr¹⁰, E. Bica,¹¹ B. Pereira Lima Ferreira¹⁰,
 J. G. Fernández–Trincado¹², P. Westera,¹³ D. Minniti,^{6,14,15} E. R. Garro,¹⁶ O. J. Katime Santrich,¹⁷
 B. J. De Bortoli,^{8,9} S. O. Souza¹,³ L. Kerber¹⁷ and A. Pérez–Villegas¹⁸

¹Observatorio Astronómico, Universidad Nacional de Córdoba, Laprida 854, X5000BGR Córdoba, Argentina

²Instituto de Astronomía Teórica y Experimental (UNC-CONICET), Laprida 854, X5000BGR Córdoba, Argentina

³IAG, Universidade de São Paulo, Rua do Matão 1226, Cidade Universitária, São Paulo 05508-900, Brazil

⁴Astronomical Observatory, University of Warsaw, Al. Ujazdowskie 4, PL-00-478 Warszawa, Poland

⁵Centro Federal de Educação Tecnológica de Minas Gerais, Av. Monsenhor Luitz de Gonzaga, 103, 37250-000 Nepomuceno, MG, Brazil

⁶Facultad de Ciencias Exactas, Instituto de Astrofísica, Universidad Andres Bello, Av. Fernández Concha 700, Santiago, Chile

⁷Instituto de Física, Universidade Federal do Rio de Janeiro, 21941-972 Rio de Janeiro, RJ, Brazil

⁸Facultad de Ciencias Astronómicas y Geofísicas, Universidad Nacional de La Plata, Paseo del Bosque s/n, 1900 La Plata, Argentina

⁹Instituto de Astrofísica de La Plata (CCT La Plata, UNLP-CONICET), Paseo del Bosque s/n, 1900 La Plata, Argentina

¹⁰Departamento de Física, ICEx - UFMG, Av. Antônio Carlos 6627, 31270-901 Belo Horizonte, Brazil

¹¹Departamento de astronomia, Universidade Federal do Rio Grande do Sul, CP15051, Porto Alegre 91501-970, Brasil, Brazil

¹²Instituto de Astronomía, Universidad Católica del Norte, Av. Angamos 0610, Antofagasta, Chile

¹³Centro de Ciências Naturais e Humanas, Universidade Federal do ABC, Avenida dos Estados, 5001, 09210-580 Santo André, SP, Brazil

¹⁴Vatican Observatory, V00120 Vatican City State, Italy

¹⁵Departamento de Física, Universidade Federal de Santa Catarina, Trindade 88040-900, Florianópolis, Brazil

¹⁶ESO - European Southern Observatory, Alonso de Cordova 3107, Vitacura, Santiago, Chile

¹⁷Departamento de Ciências Exatas, Universidade Estadual de Santa Cruz (UESC), Rodovia Jorge Amado km 16, 45662-900 Ilhéus, Brazil

¹⁸Instituto de Astronomía, Universidad Nacional Autónoma de México, Apartado Postal 106, C. P. 22800 Ensenada, B. C., Mexico

Accepted 2023 December 11. Received 2023 November 30; in original form 2023 September 27

ABSTRACT

The structure of the Small Magellanic Cloud (SMC) outside of its main body is characterized by tidal branches resulting from its interactions mainly with the Large Magellanic Cloud (LMC). Characterizing the stellar populations in these tidal components helps to understand the dynamical history of this galaxy and of the Magellanic system in general. We provide full phase-space vector information for Southern Bridge clusters. We performed a photometric and spectroscopic analysis of twelve SMC clusters, doubling the number of SMC clusters with full phase-space vector information known to date. We reclassify the sample considering 3D distances and 3D velocities. We found that some of the clusters classified as Southern Bridge objects according to the projected 2D classification actually belong to the Main Body and Counter-Bridge in the background. The comparison of the kinematics of the genuine foreground Bridge clusters with those previously analysed in the same way reveals that Southern Bridge clusters are moving towards the LMC and share the kinematics of the Northern Bridge. Adding to our sample clusters from the literature with CaT metallicity determinations we compare the age–metallicity relation of the Southern Bridge with the one of the Northern Bridge. We reinforce the idea that both regions do not seem to have experienced the same chemical enrichment history and that there is a clear absence of clusters in the Northern Bridge older than 3 Gyr and more metal poor than -1.1 , which would not seem to be due to a selection effect.

Key words: galaxies: evolution – (*galaxies*): Magellanic Clouds – galaxies: star clusters: general.

1 INTRODUCTION

The Large and Small Magellanic Clouds (LMC and SMC, respectively) constitute one of the most interesting pairs of interacting dwarf galaxies. Due to their proximity to the Milky

Way (MW) (LMC: 49.59 ± 0.54 kpc, Pietrzyński et al. 2019; SMC: 62.44 ± 0.81 kpc, Graczyk et al. 2020) and the fact that their individual stars can be resolved, these galaxies have made it possible to study in detail not only the chemical and dynamical evolution but also how interaction tidal processes can shape the morphology of this kind of galaxies (e.g. Zivick et al. 2018; De Leo et al. 2020; Patel et al. 2020; Fernández-Trincado et al. 2020; Nidever 2023).

Numerous evidences that the Magellanic Clouds (MCs) are interacting with each other and with the MW can be found imprinted in

* E-mail: cparisi@unc.edu.ar (MCP); roliveiraastro@gmail.com (RAPO); mateusangelo@cefetmg.br (MSA); astro.bdias@gmail.com (BD)

different characteristics of their stellar populations (e.g. Dobbie et al. 2014; Subramanian et al. 2017; De Leo et al. 2020). For example, since the MCs are gas-rich galaxies, close encounters between them would have produced bursts of star and cluster formation (e.g. Glatt, Grebel & Koch 2010; Bitsakis et al. 2018; Rubele et al. 2018) and subsequent chemical enrichment (e.g. Pagel & Tautvaisiene 1998). Also, complex patterns of velocities can be observed in the stellar populations due to galaxy–galaxy interaction (e.g. Niederhofer et al. 2018; 2021; Zivick et al. 2018; James et al. 2021) and stellar overdensities are suggested to be the products of stretching and tidal stripping processes (e.g. Pieres et al. 2017; El Youssoufi et al. 2021; Cullinane et al. 2023).

Besides, several tidal trails can be found around the MCs (e.g. Mackey et al. 2018; Belokurov & Erkal 2019; Nidever et al. 2019; El Youssoufi et al. 2021; Gaia Collaboration 2021b). In the particular case of the SMC, the galaxy we will focus on in this paper, the Magellanic Bridge (e.g. Dias et al. 2021; Omkumar et al. 2021), the Counter-Bridge (e.g. Rippepi et al. 2017; Muraveva et al. 2018; Dias et al. 2021; Niederhofer et al. 2021; Omkumar et al. 2021), and the West Halo (Dias et al. 2016; Niederhofer et al. 2018; Zivick et al. 2018; Tatton et al. 2021) are examples of tidal trails, all of them located outside of the Main Body (Dias et al. 2016; Parisi et al. 2022) and interpreted as the consequences of the LMC–SMC interaction (e.g. Besla et al. 2012; Diaz & Bekki 2012). Therefore, studying the stellar populations spatially separated into these tidal components can help to understand the dynamical history of the SMC in the context of its interactions with its partner the LMC and the MW. Any theoretical model that attempts to explain the formation, evolution, and history of the MCs must be able to reproduce the properties of their stellar populations.

Star clusters are excellent tracers of all the processes that their host galaxies have undergone, and the star cluster system of the SMC is not an exception. Dias et al. (2014) first introduced the framework of analysing the properties of the star clusters separating them into samples according to the coincidence of their projected positions with the aforementioned tidal components (Main Body, Wing/Bridge, Counter-Bridge, and West Halo, see Fig. 1). This approach was subsequently applied to some works yielding interesting results (e.g. Dias et al. 2016; De Bortoli et al. 2022; Parisi et al. 2022).

In that sense, our group, as part of the international collaboration VISCACHA (VISible Soar photometry of star Clusters in tApii and Coxi HuguA) Survey¹ and its spectroscopic follow-up, has been systematically observing star clusters in the SMC outskirts in order to analyse their structures, kinematics, dynamics, and chemical evolution. The obtained photometric and spectroscopic data, using the instruments SOAR (SOuthern Astrophysical Research telescope) Adaptive Module Imager (SAMI) and Gemini Multi-Object Spectrographs (GMOS) at Gemini-S, allowed the determination of accurate distances, radial velocities (RV), ages, and metallicities of a number of clusters from the catalogue of Bica et al. (2020). Using this information, along with proper motions (PM) from *Gaia* eDR3² (Gaia Collaboration 2021a), we analysed the Magellanic Bridge, Counter Bridge (Dias et al. 2021, hereafter Paper III) and the West Halo (Dias et al. 2022, hereafter Paper IV) in the 8D parameter space (6D phase-space vector, age, and metallicity), discovering that the Bridge and Counter-Bridge are roughly aligned along the LMC–SMC direction and they are both moving away from the SMC in opposite directions along the LMC–SMC axis.

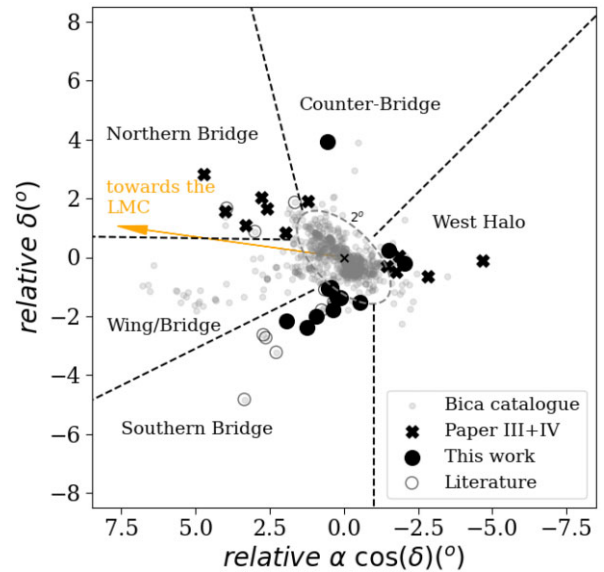


Figure 1. Distribution of SMC clusters included in this work as well as those studied previously by the VISCACHA collaboration (Paper III and Paper IV) superimposed to the objects from Bica et al. (2020) catalogue. Also clusters from the literature having CaT metallicities are included. The ellipse is used to delimit the projected location of the SMC main body. Thick dashed lines split the regions outside the main body into different 2D SMC components defined by Dias et al. (2014, 2016).

The Magellanic Bridge is a large structure that extends towards the LMC, initially thought only to contain gas and young stellar populations (Putman et al. 2003; Harris 2007). Subsequent studies revealed that there is a second branch (which we call the Southern Bridge) not aligned with the LMC and having an old stellar content traced by RR Lyrae (Belokurov et al. 2017; Jacyszyn-Dobrzniecka et al. 2017). More recently, our work about the Bridge (Paper III) provided an even more interesting scenario, showing the existence of a third branch (see also some initial partial evidence by Nidever et al. 2013; Omkumar et al. 2021). This third branch (which we refer to as Northern Bridge) would be traced by star clusters that move from the SMC towards the LMC. We marked in Fig. 1 the projected location on the sky of the Southern Bridge and Northern Bridge, as well as the other previously mentioned tidal components. The *N*-body simulation of Diaz & Bekki (2012) suggested that the Counter-Bridge was formed together with the Magellanic Bridge (~250 Myr ago) as its tidal counterpart. In Paper III, we found the first star cluster belonging to the Counter-Bridge. Additionally, in VISCACHA’s Paper VII (Oliveira et al. 2023) two groups of star clusters were identified: one younger (formed *in situ*) and one older (tidally dragged from the SMC) than the Magellanic Bridge.

Continuing this line of research, we now focus on the Southern Bridge. We also include two clusters from the West Halo and one cluster from the Counter-Bridge for which we have data. In Sections 2 and 3, we describe the observations, data reduction, and the procedures we employed for the cluster parameter determinations. We discuss in Section 4 the structure and kinematics of the studied cluster sample and we summarize our work and conclusions in Section 5.

¹<http://www.astro.iag.usp.br/~viscacha/>

²<https://archives.esac.esa.int/gaia>

2 OBSERVATION

The SMC clusters sample analysed in this paper includes nine clusters from the Southern Bridge, two from the West Halo and one from the Counter-Bridge, according to the classification by Dias et al. (2016). In this way we complement our previous works (Paper III and Paper IV), wherein clusters of the Wing/Bridge, Counter-Bridge, and West Halo were observed and analysed in a homogeneous way. The distribution of the clusters kinematically analysed by VISCACHA can be seen in Fig. 1. Clusters from Parisi et al. (2009, 2015) and Geisler et al. (2023) with available CaT metallicities are also included in this figure.

The photometric images were obtained with the SOAR adaptive optics module (SAM) of the SOAR 4-meter telescope in the context of the VISCACHA project, under the programmes SO2016B-015, SO2017B-014, SO2019B-019, CN2020B-001, and SO2021B-017. SAM is a ground-layer adaptive optics instrument using a Rayleigh laser guide star (at ~ 7 km from the telescope (Tokovinin et al. 2016), and was employed with its internal CCD detector (SAMI) binned into a 2×2 configuration, yielding a resolution of 0.091 arcsec pixel $^{-1}$ over its 3.1×3.1 arcmin 2 field of view. Long and short exposures were acquired for each target in the *V* and *I* filters of the Johnson–Cousins photometric system; Stetson (2000) standard star fields were also observed during each night to allow photometric calibration.

For the particular case of cluster HW 79, the obtained *I* exposure was not deep enough due to technical problems. Therefore we used the magnitudes in the *g* and *i* bands from the Survey of the MAgellanic Stellar History (SMASH;³ Nidever et al. 2017), which were obtained from Point-Spread Function Fitting photometry (PSF) performed on their pre-images using DAOPHOT (Stetson 1987). Quality control of the SMASH sources was ensured by filtering out those with DAOPHOT parameters $\text{abs}(\text{SHARP}) > 1.0$ and $\chi^2 > 3.0$, and SExtractor stellar probability < 0.8 , as instructed in Martínez-Delgado et al. (2019). An additional cut leaving only stars with three or more detections in the *g* band ($\text{ndetg} \geq 3$) was made to avoid stars located in the gaps between the Dark Energy Camera (DECam) CCDs.

On the other hand, the GMOS Trinational Project between Chile, Brazil, and Argentina is in charge of carrying out the spectroscopic follow-up of the VISCACHA Survey. Therefore, cluster pre-images in the *g* and *r* filters and spectra for a number of red giant stars in the field of the clusters have been obtained in the CaT region. The instrument GMOS on Gemini-S was used to obtain a total of ~ 370 spectra in the 12 observed clusters, under the programmes GS-2019B-Q-303, GS-2020B-Q-321, and GS-2021B-Q-134. We use the next instrumental configuration: the R831 grating, the CaT blocking filter, slits having a 1.0 arcsec width and central wavelength at ~ 8540 Å. This configuration allowed to obtain spectra with a resolution of ≈ 2000 that cover a spectral range of ~ 7345 – 9705 Å. Since the CaT technique is suitable to red giant stars (Da Costa & Hatzidimitriou 1998; Cole et al. 2004; Dias & Parisi 2020), we selected the spectroscopic targets from the cluster colour–magnitude diagrams (CMDs) red giant branches. All the relevant information about the observations are presented in Table 1.

³<https://datalab.noirlab.edu/smash/smash.php>

3 DATA REDUCTION AND CLUSTER PARAMETER DETERMINATIONS

3.1 Data reduction of photometric and spectroscopic data

Photometric data processing was performed using standard IRAF routines for mosaic CCD data reduction: MSCRED for bias subtraction and flat-field correction and CRUTIL for cosmic rays removal. Astrometric calibration was done by MSCMATCH, using the *Gaia* eDR3 catalogue as astrometric reference; typical root mean square (RMS) residuals of these calibrations are inferior to 0.1 arcsec. Exposures were then co-added into the final mosaics by using the World Coordinate System to register them to a global frame. Photometry was carried out by applying our own developed IDL code, which is based on STARFINDER (Diolaiti et al. 2000), to perform PSF photometry in all co-added exposures. Photometric calibration was done by employing a set of (Stetson 2000) standard star fields, observed nightly, and the MCPS catalogue (Magellanic Clouds Photometric Survey; Zaritsky et al. 2002), when available. More details about these procedures are explained in detail in the VISCACHA Paper I (Maia et al. 2019).

The spectroscopic GMOS/Gemini-S data were reduced with the use of dedicated IRAF tasks available in version 1.14 of the Gemini IRAF package.⁴ The detailed scripts (developed by M. Angelo) are publicly available⁵ and the general steps are briefly described here. The GMOS frames were pre-reduced with the usual procedures of bias and overscan subtraction and flat-field division (GSREDUCE task). Bad pixels across the detector’s arrays (together with the unilluminated gaps between the CCDs) were corrected by means of local linear interpolations (GMOSAIC and FIXPIX tasks) with the use of dedicated bad pixel masks. The pixel versus λ calibrations (GSWAVELENGTH task) were derived from CuAr arc-lamp spectra and the catalogued emission line lists available in the Gemini IRAF package. The RMS of the fitting residuals were typically smaller than ~ 0.05 Å (i.e. typically smaller than ~ 10 per cent of a pixel size, for an employed dispersion of 0.76 Å pix $^{-1}$). Bright emission sky lines from the list of Hanuschik (2003) were used as references along with the arc-lamps in order to properly find the absolute zero-points in the wavelength solutions.

After that, the spectra were (i) corrected for differences in quantum efficiency between the detector chips (GQECORR task), (ii) cleaned of cosmic rays with the use of the Laplacian Edge Detection algorithm (LACOSMIC task; van Dokkum 2001), (iii) corrected for distortions along the spatial direction (GSTRANSFORM task), (iv) background subtracted (GSSKYSUB task), (v) extracted to the usual flux \times wavelength format (GSEXTRACT task), and (vi) normalized to the continuum level (CONTINUUM task) by fitting low-order polynomials to the 8450 – 8710 Å spectral range.

3.2 Radial velocity measurement

Radial velocities (RVs) for the present sample were determined from cross-correlation (IRAF’s FXCOR task) between the science spectra and a set of theoretical templates taken from Paula Coelho’s library (Coelho 2014). The synthetic templates were first degraded in spectral resolution, in order to properly match the GMOS/Gemini-S science spectra ($R \approx 2000$), then converted to the same wavelength dispersion scale and finally continuum-normalized. The

⁴<https://www.gemini.edu/observing/phase-iii/reducing-data/gemini-iraf-data-reduction-software>

⁵<http://drforum.gemini.edu/topic/gmos-mos-guidelines-part-1/>

Table 1. Log of observations.

Cluster	Date	Grism/filter	Exp. time (s)	Airmass	FWHM (arcmin)
SAMI/SOAR photometry					
B 4; OGLE 317	2021-11-08	<i>V, I</i>	3 x 400, 3 x 600	1.38	0.63, 0.50
B 98ne, RZ 120	2021-11-08	<i>V, I</i>	3 x 400, 3 x 600	1.39	0.65, 0.54
BS 75	2016-11-02	<i>V, I</i>	6 x 200, 7 x 300	1.40	0.85, 0.65
BS 80	2021-11-08	<i>V, I</i>	3 x 400, 3 x 600	1.40	0.61, 0.49
ESO 51SC9	2017-10-22	<i>V, I</i>	6 x 200, 6 x 300	1.33	0.64, 0.49
HW 20; RZ 39	2016-09-27	<i>V, I</i>	6 x 200, 5 x 300	1.40	0.66, 0.44
HW 36; RZ 109	2021-11-07	<i>V, I</i>	3 x 400, 3 x 600	1.41	0.70, 0.58
HW 66; ESO 29 – 36;	2017-10-22	<i>V, I</i>	5 x 200, 5 x 300	1.44	0.77, 0.64
OGLE 307					
HW 79 ^a	–	–	–	–	–
L 14; RZ 9	2021-11-07	<i>V, I</i>	3 x 400, 3 x 600	1.36	0.64, 0.57
RZ 158	2021-11-08	<i>V, I</i>	3 x 400, 3 x 600	1.45	0.81, 0.63
RZ 107, B 94	2016-09-27	<i>V, I</i>	6 x 200, 6 x 300	1.40	0.63, 0.49
GMOS/Gemini-S pre-images					
B 4	2021-07-29	<i>g, r</i>	4 x 50, 4 x 166	1.40	0.78, 0.72
B 98ne	2019-09-27	<i>g, r</i>	4 x 50, 4 x 166	1.40	1.58, 1.30
BS 75	2019-08-06	<i>g, r</i>	4 x 50, 4 x 166	1.60	1.20, 1.08
BS 80	2019-09-04	<i>g, r</i>	4 x 50, 4 x 166	1.53	1.33, 1.22
ESO 51SC9	2021-07-29	<i>g, r</i>	4 x 50, 4 x 166	1.30	0.75, 0.72
HW 20	2019-10-06	<i>g, r</i>	4 x 50, 4 x 166	1.51	1.18, 1.16
HW 36	2019-10-06	<i>g, r</i>	4 x 50, 4 x 166	1.56	1.28, 0.94
HW 66	2019-09-27	<i>g, r</i>	4 x 50, 4 x 166	1.62	1.34, 0.96
HW 79	2019-09-27	<i>g, r</i>	4 x 50, 4 x 166	1.71	1.17, 1.10
L 14	2021-07-29	<i>g, r</i>	4 x 50, 4 x 166	1.48	0.77, 0.62
RZ 107	2019-09-26	<i>g, r</i>	4 x 50, 4 x 166	1.59	0.88, 0.85
RZ 158	2019-10-06	<i>g, r</i>	4 x 50, 4 x 166	1.64	1.31, 1.23
GMOS/Gemini-S multi-object spectroscopy					
B 4	2021-10-14	R831+CaT	4 x 902	1.39	0.92
B 98ne	2021-01-09	R831+CaT	5 x 903	1.54	0.98
BS 75	2019-12-07	R831+CaT	4 x 878	1.39	1.12
BS 80	2021-01-05	R831+CaT	4 x 903	2.19	0.82
ESO 51SC9	2021-10-15	R831+CaT	4 x 902	1.33	0.96
HW 20	2021-01-04	R831+CaT	4 x 903	1.69	0.76
HW 36	2021-01-04	R831+CaT	4 x 903	1.79	0.74
HW 66	2021-01-11	R831+CaT	4 x 903	1.64	0.85
HW 79	2020-12-24	R831+CaT	4 x 903	1.68	0.80
L 14	2021-10-15	R831+CaT	4 x 902	1.45	1.04
RZ 107	2020-12-21	R831+CaT	4 x 903	1.45	0.92
RZ 158	2020-12-25	R831+CaT	4 x 903	1.82	0.84

Note. The full width at half-maximum (FWHM) for the GMOS/Gemini-S pre-images and SAM/SOAR images were measured on the reduced and combined images. The FWHM for the spectroscopic observation is a reference in the *V* band.

^aDue to technical problems it was not possible to obtain a deep *I* image for HW 79. For this cluster photometry from the SMASH Survey was used (see text for details).

selected models present $\log(g) = 1.0$ and $4700 \leq T_{\text{eff}}(K) \leq 5300$, values that are representative of stars in the red giant branch phase. We also allowed for a relatively large range in metallicity ($-1.3 \leq [\text{Fe}/\text{H}] (\text{dex}) \leq -0.5$), totalizing 12 templates with these selection criteria.

For each *science–template* comparison, individual RV values are derived from fitting the peak of the cross-correlation function. The final RV of each star, together with its associated uncertainty, corresponds to the mean value obtained with the ensemble of synthetic templates.

3.3 Spectroscopic metallicity determination

The equivalent widths (EWs) of the CaT lines were measured from the spectra in the rest frame by fitting a Gaussian plus Lorentzian functions to the line profiles (Cole et al. 2004). We followed the

prescriptions of Dias & Parisi (2020) and built the CaT index as the sum of the EWs of the three CaT lines, $\Sigma\text{EW} = \text{EW}_{8498} + \text{EW}_{8542} + \text{EW}_{8662}$. Most of the spectra have a high enough signal to noise ratio (between 30 and 100) to be able to correctly fit the three lines. However, in a few cases, the weakest line is not adequately defined to make a satisfactory fit. In such cases the CaT index was computed from the EWs of the two most intense lines ($\Sigma\text{EW} = \text{EW}_{8542} + \text{EW}_{8662}$) and then corrected, according to equation (5) of Dias & Parisi (2020), to the value it would have if the three lines could have been measured. The ΣEW was also corrected for the effects of temperature and surface gravity through the reduced equivalent width (W'), which is a direct indicator of metallicity (Da Costa 1991). We use equation (4) and the value of the slope in the *r* filter, $\beta_r = 0.67 \pm 0.07$, from Dias & Parisi (2020) to calculate the W' of each observed star. The *r* versus *g* – *r* CMDs and our own python script allowed us to derive the horizontal branch level (see

Dias & Parisi 2020 for details). Finally, metallicities were calculated with equation (8) from Dias & Parisi (2020).

For the membership selection, we followed the methodology inherited from Grocholski et al. (2006) that combines RVs, metallicities, and distances of the observed stars to the centre of the corresponding cluster. The empirical cluster size adopted here is its tidal radius (r_t), derived by us following the procedure described below. On the other hand, we have adopted the same cuts in RV ($\pm 10 \text{ km s}^{-1}$) and metallicity ($\pm 0.20 \text{ dex}$) as in our previous works. Stars that lie outside the distance, RV, and metallicity cuts are coloured in Fig. A1 in blue, cyan, and green, respectively, and have been discarded as likely cluster members. We consider as cluster members those stars that are consistent with the three cuts and they are identified by red symbols in Fig. A1.

The cluster's structural parameters are derived from the fitting of the King (1962) model to the radial density profile (RDP). The RDPs were built following the procedure described in detail in Paper I. The method is based on completeness-corrected stellar counts (e.g. Maia, Moraux & Joncour 2016) in annular bins of several sizes using the calibrated V and I images, except for the cluster HW 79 for which only the V image was used, due to the reasons explained in Section 2. The RDPs and the results are shown in Fig. A2 as well as the corresponding fitted King functions (dashed lines). Also, the derived background/foreground stellar density (σ_0) and the core and tidal radii (r_1 and r_c , respectively) are specified in the figures.

In Table 2 we present, for each cluster in our sample, the mean RV and metallicity (together with the corresponding errors) determined from those stars identified as cluster members according to our analysis.

3.4 Statistical decontamination and isochrone fitting

For the statistical decontamination, which assigns photometric membership probability to each star, we used the method described in detail in Maia, Corradi & Santos (2010). This is the same procedure that we have used in all previous VISCACHA works: Paper I, Paper III, Paper IV, Paper V (Bica et al. 2022); Paper VII and Paper VIII (Saroon et al. 2023). The CMD of a nearby control field is compared with the CMD of the cluster, both having similar densities and reddening. The CMDs are properly binned into a uniform grid of cells, in which the local density of stars are compared. The expected number of members and the membership probability are derived from the overdensity of stars within a given cluster cell relative to the corresponding field cell and from the distances of these stars from the cluster centre. This process is iterated using several grid configurations to obtain the final membership values.

The SIRIUS code (Souza et al. 2020) was employed to fit the decontaminated CMDs using PARSEC isochrones (Bressan et al. 2012) through a Bayesian approach based on the Markov chain Monte Carlo sampling method. The likelihood function of each star consists of a χ^2 in each CMD axis to find the best-fitting isochrones, including the photometric errors. Three other quantities are also considered: the membership value (stars with higher membership have a higher weight), the number of neighbour stars on the CMD (smaller weight for regions containing more stars), and a set of priors. A prior distribution can be introduced for any well-known feature or parameter to better constrain the parameter space and overcome degeneracies. In the present case, we used both the observed red clump locus and the [Fe/H] derived from the CaT analysis as Gaussian priors, as done in Paper III and Paper IV. The latter one is applied with a fixed standard deviation of 0.20 dex in order to not constrain too much the posterior distributions. In

general, the [Fe/H] prior is consistent with the final solution, but those clusters with discrepant metallicities, even considering uncertainties, are indications that a compromise between a more metal-rich CMD shape and the CaT value is found.

In Table 2, we list for each studied cluster the parameters resulting from the isochrone fits. CMDs for our sample cluster and the corresponding corner plots with the likelihood distributions are presented in Figs A3 and A4. Metallicity, being a common parameter between photometric and spectroscopic procedures, is an excellent point of comparison that allows quantifying the quality of photometric fits. As it is possible to see in Table 2, there is a systematic offset between the metallicity values determined by both methods. There are many sources of uncertainties in the model isochrones that may be contributing to the observed metallicity difference between photometry and spectroscopy, for example the mixing length (Joyce & Chaboyer 2018), rotation (Maeder & Meynet 2000; Nguyen et al. 2022), overshooting, and atomic diffusion (Cassisi, Salaris & Bono 2002). The mean difference between $[\text{Fe}/\text{H}]_{\text{CaT}}$ and $[\text{Fe}/\text{H}]_{\text{CMD}}$ is 0.13 with a standard deviation of 0.08. This value is smaller than the mean error in the determination of the metallicity of the individual stars (0.20 dex) which corresponds to the metallicity cuts adopted in our membership analysis. Therefore the agreement between the photometric and spectroscopic determinations is good. In all subsequent analysis, we decided to use the CaT metallicities.

3.5 Proper motions

For each cluster in the sample, we downloaded the PMs and parallax data from the *Gaia* eDR3 catalogue. We centred our search on the cluster's coordinates using a radius of 5 arcmin. In this way, we cover an area larger than the one of the clusters, according to the tidal radii determined by us (see Table 2 and Fig. A2). We built the Vector Point Diagrams for the 12 clusters, which are shown in Fig. A5. As in our previous papers, we selected stars with the criteria as constructed from Vasiliev (2018), but with a more relaxed constraint on PM errors to establish a better compromise between statistics and uncertainties. We selected stars with $\sigma_{\mu_\alpha} < 0.35 \text{ mas yr}^{-1}$, $\sigma_{\mu_\delta} < 0.35 \text{ mas yr}^{-1}$, and $\pi < 3\sigma_\pi$, equivalent to parallaxes consistent with zero. In the figures, the stars available in *Gaia* eDR3 within the cluster radius, that fit our selection criteria, are shown with coloured symbols according to their distance to the corresponding cluster centre. Spectroscopic targets that are cluster members according to our membership procedure are marked (black circles) as well as their average PMs weighted by the individual PM errors (red arrows). The adopted mean PMs (red crosses) are compared with the ones of the SMC and Magellanic Bridge regions (see Paper III for details about the determination of these regions). All identified spectroscopic cluster members present the *Gaia* Renormalized Unit Weight Error parameter smaller than 1.4, which is an indicative of a good astrometric solution (Lindgren et al. 2021).

3.6 Comparison with previous determinations

All clusters from our sample have been previously investigated by other authors, but not in an homogeneous way, that is one of the goals of this work. In Table 3, we have summarized the parameters that can be found in the literature so that the reader can make a detailed comparison of our determinations with those made by other works. In this paper, we have derived for the first time the [Fe/H] values for the clusters RZ 107 and B 98ne and the distance of the clusters RZ 107, B 98ne, HW 36, and ESO 51SC9. All our cluster

Table 2. Derived parameters for the star clusters. (1) Cluster name; (2) and (3) (α , δ) coordinates from Bica et al. (2020); (4) and (5) coordinates relative to the SMC centre; (6) deprojected angular distance from the SMC centre a following the definition by Dias et al. (2014); (7) classification from Dias et al. (2014, 2016) (2D) and from Paper III and Paper IV (3D); (8) number of member stars and observed stars corresponding to the GMOS/Gemini-S spectroscopy; (9) and (10) RV_{hel} and $[\text{Fe}/\text{H}]_{\text{CaT}}$ from GMOS/Gemini-S spectra; (11)–(14) age, $[\text{Fe}/\text{H}]$, $E(B - V)$, distance from VISCACHA CMD isochrone fitting; (15)–(18) $[\mu_{\alpha} \cdot \cos(\delta), \mu_{\delta}]$ PMs from *Gaia* eDR3 with their respective dispersions $\sigma_{\mu_{\alpha}}$ and $\sigma_{\mu_{\delta}}$; (19) cluster tidal radius (r_t).

Cluster	α_{J2000} (hh:mm:ss.s)	δ_{J2000} (dd:mm:ss)	α_{rel} (deg)	δ_{rel} (deg)	a (deg)	2D/3D class ^a
(1)	(2)	(3)	(4)	(5)	(6)	(7)
B 4	00:24:54.3	−73:01:50	−2.03	−0.20	3.032	WH/MB
B 98ne	01:00:28.8	−73:52:32	0.54	−1.05	2.267	SB/B
BS 75	00:54:30.9	−74:11:07	0.04	−1.36	2.264	SB/MB
BS 80	00:56:12.6	−74:09:24	0.24	−1.33	2.345	SB/MB
ESO 51SC9	00:58:58.0	−68:54:55	0.56	3.91	5.701	CB/CB
HW 20	00:44:48.0	−74:21:46	−0.54	−1.53	2.033	SB/MB
HW 36	00:59:03.7	−73:50:30	0.44	−1.01	2.092	SB/B ^b
HW 66	01:12:05.1	−75:11:51	1.24	−2.37	5.158	SB/B
HW 79	01:22:48.0	−75:00:06	1.94	−2.17	5.825	SB/B
L 14	00:32:41.0	−72:34:53	−1.50	0.25	2.628	WH/CB
RZ 107	00:58:14.8	−74:36:32	0.37	−1.78	3.195	SB/CB
RZ 158	01:06:45.1	−74:49:58	0.92	−1.99	4.201	SB/B
Cluster	$N_{\text{mem}}/N_{\text{obs}}$	RV_{hel} (km s ^{−1})	$[\text{Fe}/\text{H}]_{\text{CaT}}$ (dex)	Age (Gyr)	$[\text{Fe}/\text{H}]_{\text{CMD}}$ (dex)	$E(B - V)$ (mag)
(cont.)	(8)	(9)	(10)	(11)	(12)	(13)
B 4	4/29	200.4 ± 3.0(6.0)	−0.99 ± 0.05(0.11)	2.3 ± 0.1	−0.75 ± 0.17	0.10 ± 0.05
B 98ne	5/35	186.7 ± 3.1(7.0)	−0.96 ± 0.05(0.11)	3.5 ± 0.5	−0.81 ± 0.16	0.09 ± 0.04
BS 75	2/38	196.0 ± 7.3(10.3)	−0.99 ± 0.10(0.14)	2.4 ± 0.2	−0.84 ± 0.11	0.10 ± 0.04
BS 80	4/29	160.1 ± 4.5(8.9)	−1.00 ± 0.08(0.17)	3.0 ± 0.5	−0.81 ± 0.17	0.08 ± 0.04
ESO 51SC9	7/17	142.8 ± 0.5(3.8)	−1.08 ± 0.02(0.13)	4.1 ± 0.6	−0.86 ± 0.22	0.02 ± 0.03
HW 20	3/40	161.8 ± 5.2(9.0)	−0.74 ± 0.09(0.15)	1.26 ± 0.17	−0.66 ± 0.17	0.08 ± 0.05
HW 36	3/39	154.4 ± 3.7(6.5)	−0.84 ± 0.14(0.23)	2.8 ± 0.7	−0.84 ± 0.16	0.05 ± 0.06
HW 66	8/25	182.1 ± 1.1(3.0)	−1.16 ± 0.04(0.11)	4.0 ± 0.5	−1.06 ± 0.22	0.16 ± 0.04
HW 79	17/31	176.2 ± 0.9(3.7)	−1.26 ± 0.03(0.12)	4.9 ± 0.2	−1.04 ± 0.12	0.08 ± 0.02
L 14	4/20	111.7 ± 2.8(5.6)	−0.96 ± 0.07(0.11)	2.9 ± 0.2	−0.83 ± 0.11	0.03 ± 0.03
RZ 107	6/37	189.2 ± 1.2(3.0)	−0.92 ± 0.04(0.11)	2.9 ± 0.2	−0.83 ± 0.10	0.06 ± 0.04
RZ 158	4/33	160.7 ± 4.5(9.0)	−1.11 ± 0.05(0.11)	4.7 ± 1.4	−1.11 ± 0.19	0.08 ± 0.05
Cluster	d (kpc)	$\mu_{\alpha} \cdot \cos(\delta)$ (mas yr ^{−1})	$\sigma_{\mu_{\alpha}}$ (mas yr ^{−1})	μ_{δ} (mas yr ^{−1})	$\sigma_{\mu_{\delta}}$ (mas yr ^{−1})	(r_t) (arcsec)
(cont.)	(14)	(15)	(16)	(17)	(18)	(19)
B 4	61.4 ± 3.1	0.36 ± 0.07	0.05	−1.18 ± 0.08	0.07	86 ± 18
B 98ne	55.2 ± 2.5	0.99 ± 0.04	0.29	−1.30 ± 0.04	0.14	98 ± 23
BS 75	60.5 ± 2.5	0.66 ± 0.05	0.26	−1.31 ± 0.04	0.11	82 ± 14
BS 80	58.9 ± 3.3	0.54 ± 0.08	0.52	−1.19 ± 0.06	0.16	72 ± 22
ESO 51SC9	66.1 ± 3.0	0.45 ± 0.10	0.16	−1.30 ± 0.09	0.22	139 ± 9
HW 20	58.9 ± 4.3	0.55 ± 0.07	0.29	−1.24 ± 0.06	0.02	35 ± 12
HW 36	58.1 ± 4.3	0.76 ± 0.23	0.00	−1.37 ± 0.25	0.00	27 ± 6
HW 66	57.5 ± 2.4	0.83 ± 0.08	0.40	−0.99 ± 0.08	0.23	82 ± 3
HW 79	56.5 ± 1.1	1.19 ± 0.03	0.23	−1.42 ± 0.03	0.25	133 ± 34
L 14	69.8 ± 2.3	0.40 ± 0.09	0.04	−1.21 ± 0.09	0.00	122 ± 11
RZ 107	67.9 ± 3.4	0.50 ± 0.07	0.21	−1.14 ± 0.06	0.19	55 ± 12
RZ 158	56.0 ± 4.4	0.84 ± 0.07	0.24	−1.20 ± 0.07	0.16	68 ± 11

^aWH: West Halo, MB: Main Body, SB: Southern Bridge, CB: Counter-Bridge, B: Bridge.

^bOnly one spectroscopic member star of cluster HW 36 has PMs from *Gaia*, therefore its movement, and therefore its 3D classification, must be considered with caution.

sample have previous age determinations. All the works listed in Table 3 are based on photometric data, therefore this constitutes the first spectroscopic study for all clusters in our sample. Consequently we have determined unprecedented spectroscopic metallicities and RVs for these objects.

Some clusters in our sample have been previously photometrically studied using the same data but applying different methods to the one in this work, or the same method with minor differences (HW 20 in Paper I, RZ 158 in Paper V, B 4 and L 14 in Paper VIII). In what

follows we will make a small comparison of our results with those found in previous works of the VISCACHA collaboration.

HW 20: In Paper I, the r_t determined for this cluster (37 ± 11 arcsec) is in excellent agreement with the value derived in this work (35 ± 12 arcsec), which is expected considering that the same method for the radial profile fitting was used. Also in Paper I, the age, metallicity, reddening, and distance were derived for this cluster (see Table 3) via the Markov Chain Monte Carlo technique in a Bayesian framework on a synthetic simple stellar population CMD built using PARSEC isochrones (Bressan et al. 2012). As can

Table 3. Literature parameters for our cluster sample.

Cluster	[Fe/H]	Age (Gyr)	$E(B - V)$ (mag)	d (kpc)	Ref.
(1)	(2)	(3)	(4)	(5)	(6)
BS 75	-0.48 ± 0.26	2.51	0.03 ± 0.01	59.70	Perren, Piatti & Vázquez (2017)
	–	1.26	0.05	–	Glatt, Grebel & Koch (2010)
	–	1.78	0.00	–	Maia, Piatti & Santos (2014)
RZ 107	–	$1.37^{+2.08}_{-0.01}$	–	–	Rafelski & Zaritsky (2005)
HW 79	-0.88 ± 0.65	6.31	0.01 ± 0.01	63.68	Perren, Piatti & Vázquez (2017)
	$-1.30/-1.40 \pm 0.2$	$5.00 \pm 1.30/4.30 \pm 1.20$	$0.06/0.07$	–	Piatti et al. (2011)
B 98ne	–	4.10 ± 0.50	–	–	Parisi et al. (2014)
	–	$1.40^{+5.77}_{-0.35}$	–	–	Rafelski & Zaritsky (2005)
RZ 158	–	$7.27^{+2.73}_{-0.18}$	–	–	Rafelski & Zaritsky (2005)
	$-0.90^{+0.43}_{-0.39}$	$4.80^{+1.60}_{-1.30}$	0.06	54.70 ± 3.5	Paper V
HW 20	–	$5.69^{+4.32}_{-0.41}$	–	–	Rafelski & Zaritsky (2005)
	$-0.55^{+0.13}_{-0.10}$	$1.10^{+0.08}_{-0.14}$	$0.07^{+0.02}_{-0.01}$	$62.20^{+2.50}_{-1.20}$	Paper I
HW 36	–	$1.38^{+4.90}_{-0.03}$	–	–	Rafelski & Zaritsky (2005)
	–	$1.32^{+0.72}_{-0.030}$	0.09	–	Gatto et al. (2021)
BS 80	-0.88 ± 0.65	3.98	0.020 ± 0.009	64.27	Perren, Piatti & Vázquez (2017)
	–	1.00	0.02	–	Glatt, Grebel & Koch (2010)
	–	2.82	0.00	–	Maia, Piatti & Santos (2014)
HW 66	-0.88 ± 0.65	2.82	0.02 ± 0.01	64.27	Perren, Piatti & Vázquez (2017)
	$-1.30/-1.35 \pm 0.20$	$4.00 \pm 0.90/3.50 \pm 1.00$	0.05	–	Piatti et al. (2011)
	–	3.40 ± 0.40	–	–	Parisi et al. (2014)
ESO 51SC9	–	5.20 ± 0.40	–	–	Parisi et al. (2014)
	-1.00 ± 0.15	7.00 ± 1.30	–	–	Piatti (2012)
B 4	-1.19 ± 0.24	3.8 ± 0.6	0.05 ± 0.04	66.60 ± 3.70	Dias et al. (2016)
	$-0.98^{+0.13}_{-0.12}$	$2.75^{+0.05}_{-0.25}$	0.096	$57.00^{+8.00}_{-2.00}$	Paper VIII
L 14	–	1.26	0.01	–	Glatt, Grebel & Koch (2010)
	–	$6.29^{+0.81}_{-0.59}$	–	–	Rafelski & Zaritsky (2005)
	–	$2.40^{+0.69}_{-0.16}$	0.13	–	Gatto et al. (2021)
	-1.14 ± 0.11	2.8 ± 0.4	0.03 ± 0.02	70.60 ± 1.60	Dias et al. (2016)
	-1.00 ± 0.10	$3.20^{+0.20}_{-0.40}$	0.04	$63.00^{+4.00}_{-2.00}$	Paper VIII

Note. The ages included in this table from Rafelski & Zaritsky (2005) correspond to the extinction corrected values, STARBURST model, and $Z = 0.001$.

be seen in Tables 2 and 3, there is a good agreement between the values derived by both works, considering the errors.

RZ 158: In Paper V, the same method was used as in this work for the determination of the astrophysical parameters for this cluster, but with different prior conditions, since they did not have the CaT metallicity. The parameters determined by the two independent analyses are consistent with each other. There is however a difference of 0.21 dex between the value of the metallicity determined by us and the one from Paper V, our value being more metal poor. This difference slightly exceeds our metallicity errors (0.19 dex), however it is important to note that in Paper V the errors are substantially higher ($^{+0.43}_{-0.39}$ dex), thus being compatible within 1-sigma.

B 4: Although the metallicity values derived from the CMD analysis and CaT spectroscopy showed some discrepancy in this work (0.24 dex), they are still compatible within 1.4-sigma, given their uncertainties. In Paper VIII, PARSEC isochrones were visually fitted to the statistically decontaminated CMD, finding a metallicity very close to the value from the CaT technique. The Dias et al. (2016) derived metallicity value also favours the CaT metallicity value, even though it is substantially more metal poor. Our corner plot (Fig. A4) shows that the [Fe/H] prior leads to a compromise between the CaT value and an even more metal-rich solution. The decontamination was redone compared to Paper VIII in order

to remove the large number of binaries in $V \sim 22$ mag and to better define the subgiant branch region. This strategy possibly forced the metallicity to a more metal-rich value (compared of Paper VIII and CaT), but resulted in a statistically better fitting on the CMD.

L 14: The visual fit from Paper VIII for L 14 is similar to the SIRIUS fit of this work and the resulting parameters are compatible with each other within uncertainties. The present result comes from statistical fitting and shows a good compromise among all parameters.

We note that the small changes in age and metallicity for clusters B 4 and L 14 do not change the conclusions of Paper VIII.

4 DISCUSSIONS

The structure of the SMC presents a main body and some external arms or substructures as seen in the projected distribution of star clusters (e.g. Dias et al. 2014, 2016; Parisi et al. 2022, and others). When the third dimension is added to the analysis, a more complete and complex view of the SMC outskirts appears. As pointed out in Paper III, the SMC seems to have three branches of a Bridge pointing to and moving towards the LMC on the Eastern side and a shell of star clusters moving outwards in the Western region from the North all the way down to the Southern regions, with some clusters

on the background of the bridge as well moving together with the Counter-Bridge. This observational evidence is consistent with the model predictions by Zivick, Kallivayalil & van der Marel (2021) describing the SMC with an inner cylindrical rotation and an outer tidal expansion, as well as with partial evidence showing foreground and background stellar populations by e.g. Nidever et al. (2013), Omkumar et al. (2021), and by outward proper motions by *Gaia*, the survey of the Magellanic Clouds system (VMC) using the Visual and Infrared Telescope for Astronomy (VISTA), and the Hubble Space Telescope (e.g. Niederhofer et al. 2018; Zivick et al. 2018; Piatti 2021). We have detected the alignment of these structures with the LMC–SMC direction combined with the outward motion for the first time in a self-consistent analysis of full 3D positions and motions of selected SMC star clusters in two opposite regions, the Northern Bridge (Paper III) and West Halo (Paper IV). In this work, we add the Southern Bridge region to the analysis to check whether it follows or not the Northern Bridge. In this section we discuss the structure, kinematics, and age metallicity relation (AMR) of the Southern Bridge, as traced by star clusters, in comparison with the Northern Bridge. In order to perform that comparison, we added clusters from the literature analysed with similar methods to the ones applied here to our sample, specifically, the clusters analysed in Paper III and those having CaT metallicities from the works of Parisi et al. (2009, 2015, 2022).

A first indication of the movement of the clusters in our sample are the VPDs (Fig. A5). As can be seen, considering projected distances, the two clusters catalogued by Dias et al. (2014, 2016) as West Halo (B 4 and L 14), the Counter-Bridge cluster (ESO 51SC9), and three of the nine Southern Bridge clusters (BS 80, HW 20, and RZ 107) are moving in the direction away from the LMC. In the case of the remaining six clusters, B 98ne, HW 66, and HW 79 seem to move towards the LMC while the movement of BS 75 and HW 36 is difficult to ensure due to the large uncertainties in their mean PMs. However, as shown in Paper III and Paper IV, including real distances instead of projected distances brings a more realistic picture of the kinematics and structure of the SMC traced by its star cluster system. The 2D classification originally proposed by Dias et al. (2014, 2016) was superseded by a new 3D classification defined in Paper III and Paper IV, which is based on full phase-space analysis. Clusters located within the SMC tidal radius (r_{SMC}) are considered to belong to the Main Body. The outer clusters ($r > r_{\text{SMC}}$) are classified as Bridge or Counter-Bridge according to their 3D positions and velocity directions: Bridge clusters if they are foreground clusters moving towards the LMC and Counter-Bridge if they are moving in the opposite direction, as predicted by dynamical models.

We show the 3D distribution of the star clusters in Fig. 2. We consider a sphere of 4 kpc as representative of the r_{SMC} for the SMC. As can be seen, the sky regions Southern Bridge, West Halo, and Counter-Bridge analysed in this work contain: five clusters (HW 36, B 98ne, RZ 158, HW 66, and HW 79) following the structure of the Northern Bridge sample analysed in Paper III and represented in Fig. 2 with orange crosses; four clusters (B 4, HW 20, BS 75, and BS 80) from the Main Body with distances similar to the SMC centre; and three background cluster (RZ 107, L 14, and ESO 51SC9) which means that they are consistent with the 3D Counter-Bridge shell moving outwards found in Paper IV.

That reinforces, despite the low number of clusters, the suggestion of Tatton et al. (2021) and Paper IV that the West Halo clusters belong to the Counter-Bridge, and perhaps also to the Main Body. On the other hand, the only 2D Counter-Bridge cluster (ESO 51SC9) in our sample is confirmed to belong to the Counter-Bridge according to the 3D classification. As can be seen in Fig. 2, the five Bridge clusters

and the three Counter-Bridge clusters, reclassified in this work, follow the velocity patterns of their neighbours in the corresponding components. Also in Fig. 2 it is evident that, in the planes that involve the distance, Southern Bridge, and Northern Bridge clusters appear to follow the same tail from the SMC, but being the Southern Bridge ones closer to the SMC main body in the line of sight.

The kinematics of the full sample is shown in Fig. 3 as a direct comparison with the simulated stellar particles from Diaz & Bekki (2012). The plots reinforce the idea that the five genuine Bridge clusters studied in this work follow the kinematics of the Northern Bridge, also confirming that the Southern Bridge is moving towards the LMC. Besides, the three clusters reclassified here as Counter-Bridge clusters show kinematics consistent with the shell moving outwards in the opposite direction to the Bridge, also reinforcing the suggestion of Paper IV that the Counter-Bridge forms a ring in the boundary of the SMC moving away from the SMC.

One aspect important to be mentioned in Fig. 3 is that the kinematics become confusing when the parameter a is used instead of the real distances. The deprojected distance a has been defined by Piatti et al. (2005) as the semi-major axis of an ellipse centred in the centre of the SMC, with axis ratio of $b/a = 1/2$, and coinciding with the position of the cluster. This is equivalent of stating that real cluster positions are in a circular disc. However, new evidence (e.g. Zivick, Kallivayalil & van der Marel 2021) consolidates that the SMC cannot be described simply by a disc. Also, in Paper IV we show that the metallicity and age radial gradients can be observed when the deprojected distance a is used but they vanish when real 3D distances are considered, showing that they are not real. So, this parameter is not appropriate to accurately perform any analysis involving distances and positions of the clusters. Both aforementioned VISCACHA's previous works and this paper clearly demonstrate that the use of the parameter a as an indicator of distance is dispensable in future analyses. To make the necessary effort to determine real distances, as the VISCACHA collaboration has been systematically doing, is mandatory.

In general terms, the 3D distribution and 3D kinematics of the star clusters presented in this work are comparable to the predictions from the simulations of Diaz & Bekki (2012). However, the simulations are not able to reproduce a couple of smaller scale details, for example: (i) there is not evident overdensity of stars to characterize the Northern and Southern Bridge, and the gas particles show an overdensity for the young bridge and counter-bridge, which does not match with the intermediate-age clusters discussed here; (ii) the kinematics of the foreground bridge stars and gas shows a clear pattern that is similar in the simulations and data, but this does not seem to be the case for the background counter-bridge clusters. We stress that these are the most recent simulations of the entire Magellanic System orbits around the Milky Way reaching this level of details of small-scale structure of the SMC including structure and kinematics. However, this model is more than 10 yr old, and since then the LMC mass determination has shown that the LMC is a factor of 10 heavier, favouring the first infall scenario proposed by Besla et al. (2007). The full simulations of Besla et al. (2010, 2012) are focused on the large scale-structure of the Magellanic System and does not provide an SMC small-scale structure comparable with observations, which was the focus of more recent models by Zivick, Kallivayalil & van der Marel (2021) for example, but without the full simulation of the LMC, SMC orbit. We expect that the accumulating evidence from the VISCACHA star clusters can serve as hard constraints for forthcoming full chemo-dynamical simulations that are timely and necessary.

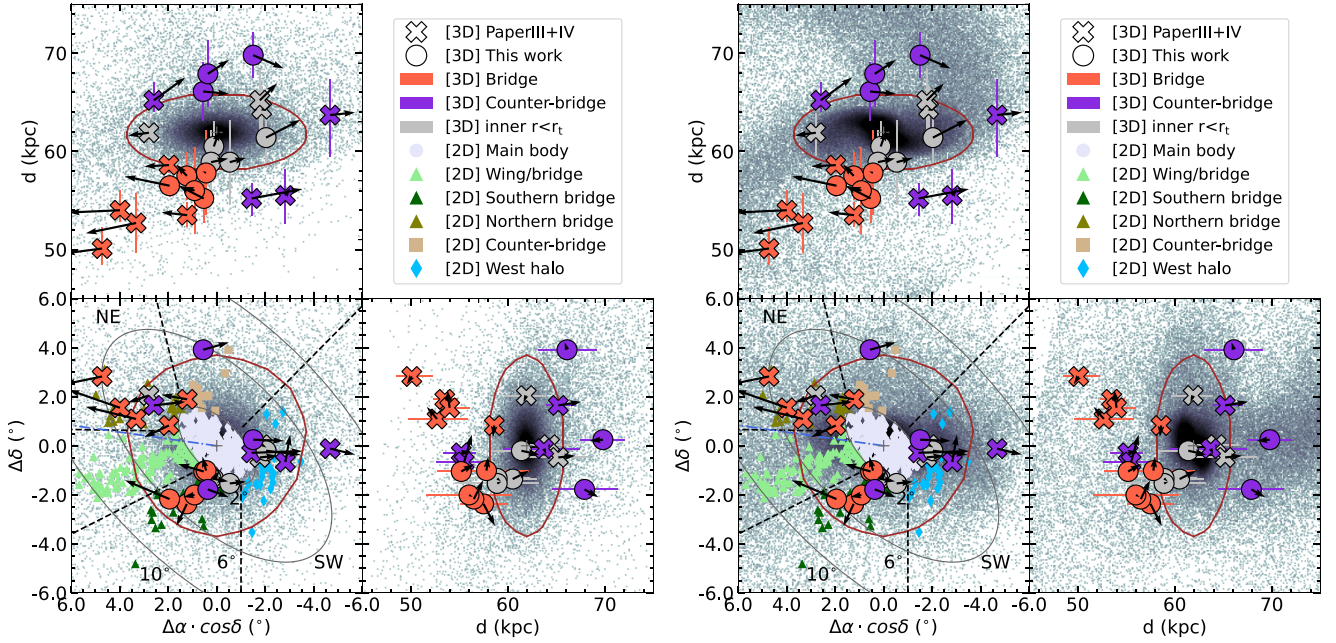


Figure 2. 3D distribution of the star clusters analysed in this paper combined with the previous sample. Cross symbols are clusters from the two previous works and the circles are the additions from this work. Colours indicate their classification according to Paper III whereas the 2D projected regions defined by Dias et al. (2014, 2016, 2021) have smaller symbols in the bottom left panel only. The brown circles and ellipses are the projections of a sphere of radius 4 kpc around the SMC centre representative of the SMC tidal radius. Blue ellipse represents the break radius from Paper III. Left and right sets of panels contain exactly the same observational data, the difference is the background simulations by Diaz & Bekki (2012) and are shown for comparison. Left panels contain stellar particles from the spheroid component and right panels contain the gas particles from the disc component from the same simulation.

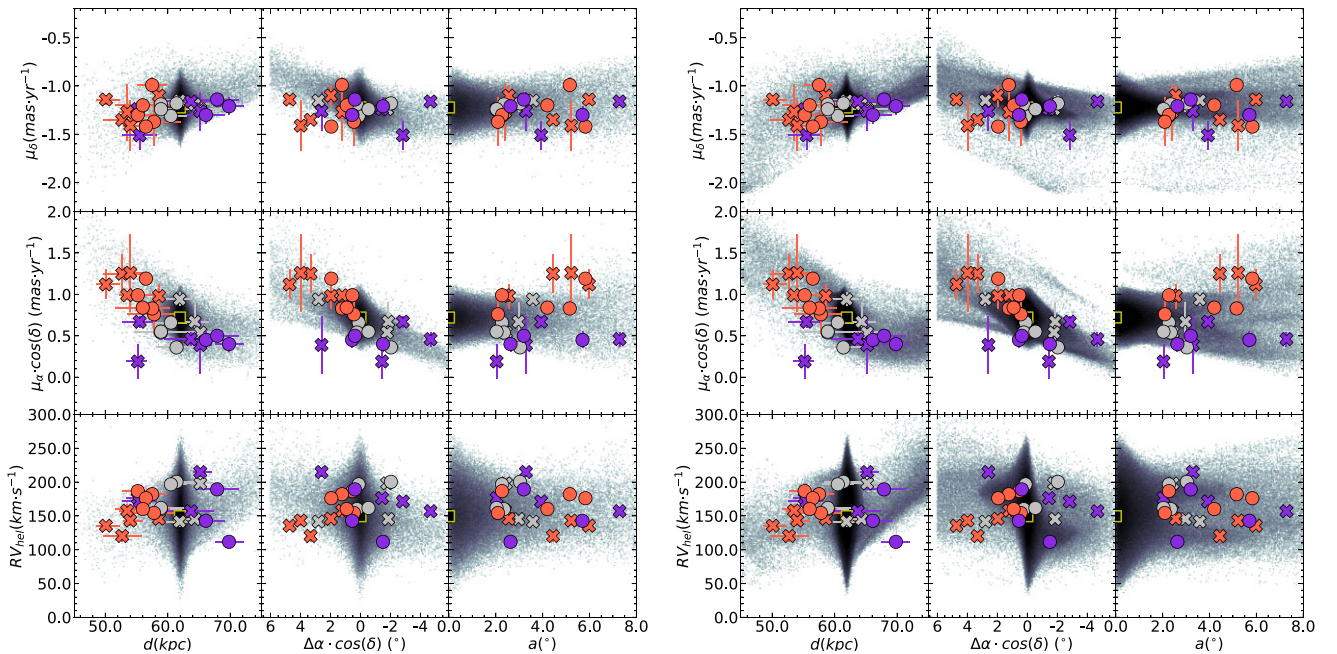


Figure 3. Kinematics of the star clusters analysed in this paper combined with the previous sample from Paper III and Paper IV. Symbols and colours are the same as defined in Fig. 2. Background particles are simulated stellar particles from the spheroid component (left panel) and gas particles (right panel) from Diaz & Bekki (2012) for comparison.

As mentioned above, since the Southern Bridge and Northern Bridge clusters are located in different regions of the sky but share the same kinematics, it is interesting to analyse whether or not they share the same chemical evolution. In Fig. 4, we compare

the behaviour of the CaT metallicity as a function of age for clusters in both components. The age and metallicity values of the additional CaT sample are listed in Table 4. In Parisi et al. (2022), the SMC AMR was analysed using all the clusters having CaT at that

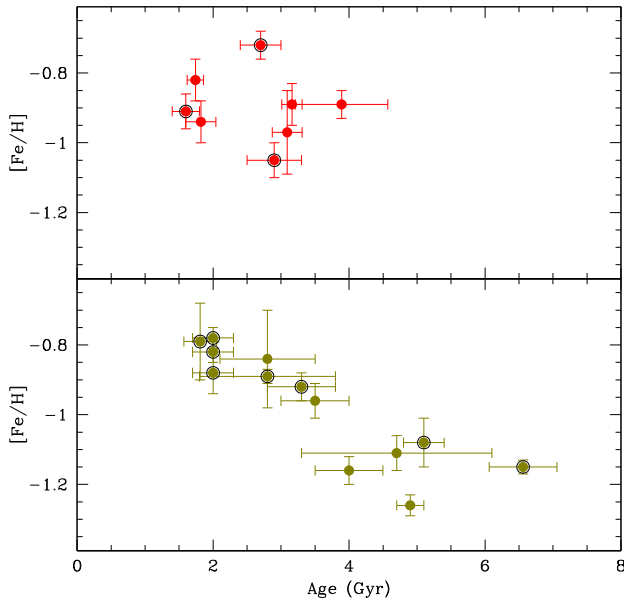


Figure 4. Age-metallicity relation of clusters with CaT metallicities. Clusters from the Southern Bridge and the Northern Bridge are shown in the bottom and top panels, respectively. Clusters taken from the literature not studied by VISCACHA (Table 4), are marked with black open circles.

Table 4. Clusters from the literature with CaT metallicities.

Cluster	Age (Gyr)	Ref.	[Fe/H]	Ref.	2D Class ^a
(1)	(2)	(3)	(4)	(5)	(6)
HW 84	1.60 ± 0.20	1	-0.91 ± 0.05	6	NB
HW 67	2.70 ± 0.30	1	-0.72 ± 0.04	7	NB
L 108	2.90 ± 0.40	1	-1.05 ± 0.05	6	NB
K 44	2.00 ± 0.30	2	-0.78 ± 0.03	8	SB
L 116	2.80 ± 1.00	3	-0.89 ± 0.02	8	SB
NGC 339	6.56 ± 0.50	4	-1.15 ± 0.02	8	SB
HW 47	3.30 ± 0.50	1	-0.92 ± 0.04	6	SB
L 58	1.81 ± 0.24	4	-0.79 ± 0.11	7	SB
L 106	2.00 ± 0.30	1	-0.88 ± 0.06	6	SB
L 112	5.10 ± 0.30	1	-1.08 ± 0.07	7	SB
L 111	2.00 ± 0.30	1	-0.82 ± 0.03	6	SB

Note. References: (1) Parisi et al. (2014); (2) Gatto et al. (2021); (3) Piatti et al. (2001); (4) Lagioia et al. (2019); (5) Paper VII; (6) Parisi et al. (2009); (7) Parisi et al. (2015); (8) Parisi et al. (2022).

^aThe 3D classification for this cluster sample is not available.

moment splitting the sample into different subsamples considering the 2D classification. Two of the Northern Bridge clusters used in Parisi et al. (2022) belong in fact to the Main Body (B 168) and to the Counter-Bridge (L 102) according to the 3D classification (Paper III) and therefore we do not consider them here. On the other hand, we add five Southern Bridge clusters to the eight ones included in Parisi et al. (2022). As can be observed in Fig. 4, this improved sample of clusters corroborates that the Southern Bridge presents a clear AMR: clusters show a trend in the sense that the material from which the clusters have been formed between 6.5 and 2 Gyr ago has been enriched from -1.2 to -0.8 dex, being the metallicity dispersion at any given age very small. In contrast, the Northern Bridge clusters cover a substantially large range in metallicities (~ 0.4 dex) occupying a small range of ages (~ 3 Gyr),

which reinforces the idea that this region, apparently, does not show a clear chemical enrichment between 4 and 2 Gyr ago, which is the age range covered by the current sample. If we only consider clusters younger than ~ 4 Gyr the mean metallicity of the Northern and Southern Bridge regions are -0.90 and -0.86 dex, respectively. Both regions present statistically consistent mean metallicities being the intrinsic metallicity dispersion (i.e. uncertainties removed) slightly larger in the Northern Bridge (0.10 dex) than in the Southern Bridge (0.06 dex). This result is expected considering that both populations cover a similar range of metallicities, but it does not reflect the trend and lack of trend shown in Fig. 4 for Southern Bridge and Northern Bridge, respectively. We note that clusters from Table 4 do not have distances and 3D classification, therefore the final AMR from Fig. 4 may or may not slightly change when this info is available in the future. Nevertheless, even if we remove these clusters from Fig. 4, the Northern Bridge and Southern Bridge sample clusters still show different age distributions.

There is a clear lack of clusters in the Northern Bridge more metal poor than -1.1 and older than 4 Gyr. We believe that this cannot be due to a selection effect since we have performed a good spatial coverage of that region (see Fig. 1) and we have not applied any selection criteria that favour the youngest and most metal-rich clusters. We suggest that this evidence shows that although these two branches of the Bridge present similar kinematic characteristics, compatible with the tidal effects due to the interaction with the LMC, the Northern and Southern part of the SMC have not experienced the same history of chemical enrichment. Almeida et al. (2023, unpublished data) analysed the chemistry of field stars split in a rough estimate of line-of-sight distances and concluded that all field stars analysed in the Main Body, East, and West SMC regions share a similar chemical evolution, but the metallicity distribution (MD) is different. They concluded that the foreground Eastern stars have a similar MD as the Main body whereas the background Eastern stars have a similar MD as the Western region. Our new evidence in this work shows that two branches of the Bridge that are part of the Eastern foreground region present a clear difference in their MD, questioning the generalization of the conclusions by Almeida et al. (2023, submitted).

5 SUMMARY AND CONCLUSIONS

We present an analysis for twelve SMC star clusters located in the projected regions Southern Bridge, West Halo, and Counter-Bridge using images from the VISCACHA Survey and its spectroscopic follow-up. Images in the V and I filters and spectra in the region of the CaT lines were obtained with SAM/SOAR and GMOS/Gemini-S, respectively. We derived ages, interstellar reddening, distances, radial velocities, and metallicities for this cluster sample and complemented these parameters with proper motions from the *Gaia* eDR3 catalogue (Gaia Collaboration 2021a). All this information allowed us to derive the phase-space vectors for our cluster sample from which we analysed the 3D structure and kinematics of the SMC cluster system, complementing our similar previous works (Paper III and Paper IV), in which we study the kinematics of the regions defined in 2D as Northern Bridge and West Halo, respectively. The conclusions of this work can be summarized as follows:

- (i) Four clusters belong to the SMC Main Body, five to the Bridge, and three to the Counter-Bridge.
- (ii) The Southern Bridge is moving toward the LMC and shares the kinematics of the Northern Bridge.

(iii) The three clusters reclassified as Counter-Bridge in 3D (ESO 51SC9, L 14, and RZ 107) follow the kinematics of this component, reinforcing the discoveries of [Paper IV](#).

(iv) The Northern Bridge and the Southern Bridge seem to have suffered the same chemical enrichment history. While the Southern Bridge presents a clear AMR, clusters of the Northern Bridge cover a wide metallicity range (between ~ -0.7 and ~ -1.1), having a spread of ~ 0.4 dex, when all ages are considered. However, clusters younger than ~ 4 Gyr have similar mean metallicities values (-0.90 ± 0.10 and -0.86 ± 0.06 dex for the Northern and Southern Bridge, respectively).

(v) There is a clear lack of Northern Bridge clusters older than 4 Gyr and more metal poor than $[Fe/H] \sim -1.1$ dex in comparison with the extended sample of older and more metal-poor clusters found in the Southern Bridge region.

A next necessary step is to provide full phase-space information for clusters classified in 2D as Wing/Bridge, analyse the 3D structure of the cluster system in that tidal branch and compare its kinematics with the one of the other two branches of the Bridge. This would help to reach a more accurate understanding of the tidal nature of the Bridge as a whole and its fine structure in particular. The results of these analyses constitute important constraints to the dynamical models that attempt to understand the origin of the Bridge and the consequences of the SMC–LMC tidal interactions. The SMC outskirts remain a very interesting science case and there is still a lot to be learned from the SMC dynamical and chemical evolution history.

ACKNOWLEDGEMENTS

MCP and BD thank Sergio Vasquez for providing his script to measure EW of CaT lines. MA and BD thank German Gimeno for useful discussions on the GMOS/Gemini-S data reduction process. BD thanks Jonathan Diaz for kindly providing their simulation results from Diaz & Bekki (2012) for direct comparison with our observational results. BD thanks the Gemini SOS personnel for the pre-image data reduction and acknowledges support by ANID-FONDECYT iniciación grant no. 11221366. FFSM acknowledges financial support from Conselho Nacional de Desenvolvimento Científico e Tecnológico – CNPq (proc. 404482/2021-0) and from FAPERJ (proc. E-26/201.386/2022 and E-26/211.475/2021). This research was partially supported by the Argentinian institution SECYT (Universidad Nacional de Córdoba) and Consejo Nacional de Investigaciones Científicas y Técnicas de la República Argentina, Agencia Nacional de Promoción Científica y Tecnológica. J.G.F.-T. acknowledges support provided by Agencia Nacional de Investigación y Desarrollo de Chile (ANID) under the Proyecto Fondecyt Iniciación 2022 Agreement No. 11220340, and from the Joint Committee ESO-Government of Chile 2021 under the Agreement No. ORP 023/2021.

DM gratefully acknowledges support from the ANID BASAL projects ACE210002 and FB210003, from Fondecyt Project No. 1220724, and from CNPq Brasil Project 350104/2022-0. We appreciate the detailed evaluation carried out by the referee and her/his helpful comments.

BPLF acknowledges the financial support from CNPq (140642/2021-8). Based on observations obtained at the Southern Astrophysical Research (SOAR) telescope, which is a joint project of the Ministério da Ciência Tecnologia e Inovações (MCTI/LNA) do Brasil, the US National Science Foundation’s NOIRLab, the

University of North Carolina at Chapel Hill (UNC), and Michigan State University (MSU).

Based on observations obtained at the international Gemini Observatory, a programme of NSF’s NOIRLab, which is managed by the Association of Universities for Research in Astronomy (AURA) under a cooperative agreement with the National Science Foundation on behalf of the Gemini Observatory partnership: the National Science Foundation (United States), National Research Council (Canada), Agencia Nacional de Investigación y Desarrollo (Chile), Ministerio de Ciencia, Tecnología e Innovación (Argentina), Ministério da Ciência, Tecnologia, Inovações e Comunicações (Brazil), and Korea Astronomy and Space Science Institute (Republic of Korea).

This work presents results from the European Space Agency (ESA) space mission *Gaia*. *Gaia* data are being processed by the Gaia Data Processing and Analysis Consortium (DPAC). Funding for the DPAC was provided by national institutions, in particular the institutions participating in the *Gaia* MultiLateral Agreement (MLA). The *Gaia* mission website is <https://www.cosmos.esa.int/gaia>. The *Gaia* archive website is <https://archives.esac.esa.int/gaia>.

DATA AVAILABILITY

The data underlying this article are available in the NOIRLab Astro Data Archive (<https://astroarchive.noirlab.edu/>) or upon request to the authors.

REFERENCES

- Almeida A. et al., 2023, preprint ([arXiv:2308.13631](https://arxiv.org/abs/2308.13631))
- Belokurov V. A., Erkal D., 2019, *MNRAS*, 482, L9
- Belokurov V., Erkal D., Deason A. J., Koposov S. E., De Angeli F., Evans D. W., Fraternali F., Mackey D., 2017, *MNRAS*, 466, 4711
- Besla G., Kallivayalil N., Hernquist L., Robertson B., Cox T. J., van der Marel R. P., Alcock C., 2007, *ApJ*, 668, 949
- Besla G., Kallivayalil N., Hernquist L., van der Marel R. P., Cox T. J., Kereš D., 2010, *ApJ*, 721, L97
- Besla G., Kallivayalil N., Hernquist L., van der Marel R. P., Cox T. J., Kereš D., 2012, *MNRAS*, 421, 2109
- Bica E., Westera P., Kerber L. d. O., Dias B., Maia F., Santos Jr J. F. C., Barbay B., Oliveira R. A. P., 2020, *AJ*, 159, 82
- Bica E. et al., 2022, *MNRAS*, 517, L41
- Bitsakis T., González-Lópezlira R. A., Bonfina P., Bruzual G., Maravelias G., Zaritsky D., Charlot S., Ramírez-Siordia V. H., 2018, *ApJ*, 853, 104
- Bressan A., Marigo P., Girardi L., Salasnich B., Dal Cero C., Rubele S., Nanni A., 2012, *MNRAS*, 427, 127
- Cassisi S., Salaris M., Bono G., 2002, *ApJ*, 565, 1231
- Coelho P. R. T., 2014, *MNRAS*, 440, 1027
- Cole A. A., Smecker-Hane T. A., Tolstoy E., Bosler T. L., Gallagher J. S., 2004, *MNRAS*, 347, 367
- Cullinane L. R., Mackey A. D., Da Costa G. S., Koposov S. E., Erkal D., 2023, *MNRAS*, 518, L25
- Da Costa G. S., 1991, in Haynes R., Milne D. eds, Proc. IAU Symp. 148, The Magellanic Clouds. Kluwer, Dordrecht, p. 183
- Da Costa G. S., Hatzidimitriou D., 1998, *AJ*, 115, 1934
- De Bortoli B. J., Parisi M. C., Bassino L. P., Geisler D., Dias B., Gimeno G., Angelo M. S., Mauro F., 2022, *A&A*, 664, A168
- De Leo M., Carrera R., Noël N. E. D., Read J. I., Erkal D., Gallart C., 2020, *MNRAS*, 495, 98
- Dias B., Parisi M. C., 2020, *A&A*, 642, A197
- Dias B., Kerber L. O., Barbay B., Santiago B., Ortolani S., Balbinot E., 2014, *A&A*, 561, A106
- Dias B., Kerber L., Barbay B., Bica E., Ortolani S., 2016, *A&A*, 591, A11
- Dias B. et al., 2021, *A&A*, 647, L9 (Paper III)
- Dias B. et al., 2022, *MNRAS*, 512, 4334 (Paper IV)
- Diaz J. D., Bekki K., 2012, *ApJ*, 750, 36

- Diolaiti E., Bendinelli O., Bonaccini D., Close L., Currie D., Parmeggiani G., 2000, *A&AS*, 147, 335
- Dobbie P. D., Cole A. A., Subramaniam A., Keller S., 2014, *MNRAS*, 442, 1663
- El Youssoufi D. et al., 2021, *MNRAS*, 505, 2020
- Fernández-Trincado J. G. et al., 2020, *ApJ*, 903, L17
- Gaia Collaboration, 2021a, *A&A*, 649, A1
- Gaia Collaboration, 2021b, *A&A*, 649, A7
- Gatto M. et al., 2021, *MNRAS*, 507, 3312
- Geisler D. et al., 2023, *A&A*, 669, A115
- Glatt K., Grebel E. K., Koch A., 2010, *A&A*, 517, A50
- Graczyk D. et al., 2020, *ApJ*, 904, 13
- Grocholski A. J., Cole A. A., Sarajedini A., Geisler D., Smith V. V., 2006, *AJ*, 132, 1630
- Hanuschik R. W., 2003, *A&A*, 407, 1157
- Harris J., 2007, *ApJ*, 658, 345
- Jacyszyn-Dobrzaniecka A. M. et al., 2017, *Acta Astron.*, 67, 1
- James D. et al., 2021, *MNRAS*, 508, 5854
- Joyce M., Chaboyer B., 2018, *ApJ*, 856, 10
- King I., 1962, *AJ*, 67, 471
- Lagioia E. P., Milone A. P., Marino A. F., Dotter A., 2019, *ApJ*, 871, 140
- Lindgren L. et al., 2021, *A&A*, 649, A2
- Mackey D., Koposov S., Da Costa G., Belokurov V., Erkal D., Kuzma P., 2018, *ApJ*, 858, L21
- Maeder A., Meynet G., 2000, *ARA&A*, 38, 143
- Maia F. F. S., Corradi W. J. B., Santos Jr J. F. C., 2010, *MNRAS*, 407, 1875
- Maia F. F. S., Piatti A. E., Santos J. F. C., 2014, *MNRAS*, 437, 2005
- Maia F. F. S., Moraux E., Joncour I., 2016, *MNRAS*, 458, 3027
- Maia F. F. S. et al., 2019, *MNRAS*, 484, 5702
- Martínez-Delgado D. et al., 2019, *A&A*, 631, A98
- Muraveva T. et al., 2018, *MNRAS*, 473, 3131
- Nguyen C. T. et al., 2022, *A&A*, 665, A126
- Nidever D. L., 2023, preprint ([arXiv:2308.05156](https://arxiv.org/abs/2308.05156))
- Nidever D. L., Monachesi A., Bell E. F., Majewski S. R., Muñoz R. R., Beaton R. L., 2013, *ApJ*, 779, 145
- Nidever D. L. et al., 2017, *AJ*, 154, 199
- Nidever D. L. et al., 2019, *ApJ*, 887, 115
- Niederhofer F. et al., 2018, *A&A*, 613, L8
- Niederhofer F. et al., 2021, *MNRAS*, 502, 2859
- Oliveira R. A. P. et al., 2023, *MNRAS*
- Omkumar A. O. et al., 2021, *MNRAS*, 500, 2757
- Pagal B. E. J., Tautvaisiene G., 1998, *MNRAS*, 299, 535
- Parisi M. C., Grocholski A. J., Geisler D., Sarajedini A., Clariá J. J., 2009, *AJ*, 138, 517
- Parisi M. C. et al., 2014, *AJ*, 147, 71
- Parisi M. C., Geisler D., Clariá J. J., Villanova S., Marconi N., Sarajedini A., Grocholski A. J., 2015, *AJ*, 149, 154
- Parisi M. C., Gramajo L. V., Geisler D., Dias B., Clariá J. J., Da Costa G., Grebel E. K., 2022, *A&A*, 662, A75
- Patel E. et al., 2020, *ApJ*, 893, 121
- Perren G. I., Piatti A. E., Vázquez R. A., 2017, *A&A*, 602, A89
- Piatti A. E., 2012, *ApJ*, 756, L32
- Piatti A. E., 2021, *A&A*, 650, A52
- Piatti A. E., Santos J. F. C., Clariá J. J., Bica E., Sarajedini A., Geisler D., 2001, *MNRAS*, 325, 792
- Piatti A. E., Santos J. F. C. J., Clariá J. J., Bica E., Ahumada A. V., Parisi M. C., 2005, *A&A*, 440, 111
- Piatti A. E., Clariá J. J., Bica E., Geisler D., Ahumada A. V., Girardi L., 2011, *MNRAS*, 417, 1559
- Pieres A. et al., 2017, *MNRAS*, 468, 1349
- Pietrzyński G. et al., 2019, *Nature*, 567, 200
- Putman M. E., Staveley-Smith L., Freeman K. C., Gibson B. K., Barnes D. G., 2003, *ApJ*, 586, 170
- Rafelski M., Zaritsky D., 2005, *AJ*, 129, 2701
- Ripepi V. et al., 2017, *MNRAS*, 472, 808
- Rubele S. et al., 2018, *MNRAS*, 478, 5017
- Saroon S. et al., 2023, *A&A*, 677, A35
- Souza S. O., Kerber L. O., Barbuy B., Pérez-Villegas A., Oliveira R. A. P., Nardiello D., 2020, *ApJ*, 890, 38
- Stetson P. B., 1987, *PASP*, 99, 191
- Stetson P. B., 2000, *PASP*, 112, 925
- Subramanian S. et al., 2017, *MNRAS*, 467, 2980
- Tatton B. L. et al., 2021, *MNRAS*, 504, 2983
- Tokovinin A., Cantarutti R., Tighe R., Schurter P., Martinez M., Thomas S., van der Blik N., 2016, *PASP*, 128, 125003
- Vasiliev E., 2018, *MNRAS*, 481, L100
- Zaritsky D., Harris J., Thompson I. B., Grebel E. K., Massey P., 2002, *AJ*, 123, 855
- Zivick P. et al., 2018, *ApJ*, 864, 55
- Zivick P., Kallivayalil N., van der Marel R. P., 2021, *ApJ*, 910, 36
- van Dokkum P. G., 2001, *PASP*, 113, 1420

APPENDIX A: FIGURES

In this Appendix, we include figures corresponding to the spectroscopic membership selection (Fig. rd) and clusters structural parameters determinations (Fig. A2), whose respective procedures can be seen in Section 3.3. Also we present the CMD isochrone fits (Fig. A3) and the corner plots (Fig. A4) for our cluster sample, which is explained in detail in Section 3.4. The Vector Point Diagrams for our cluster sample can be seen in Fig. A5 generated as described in Section 3.5.

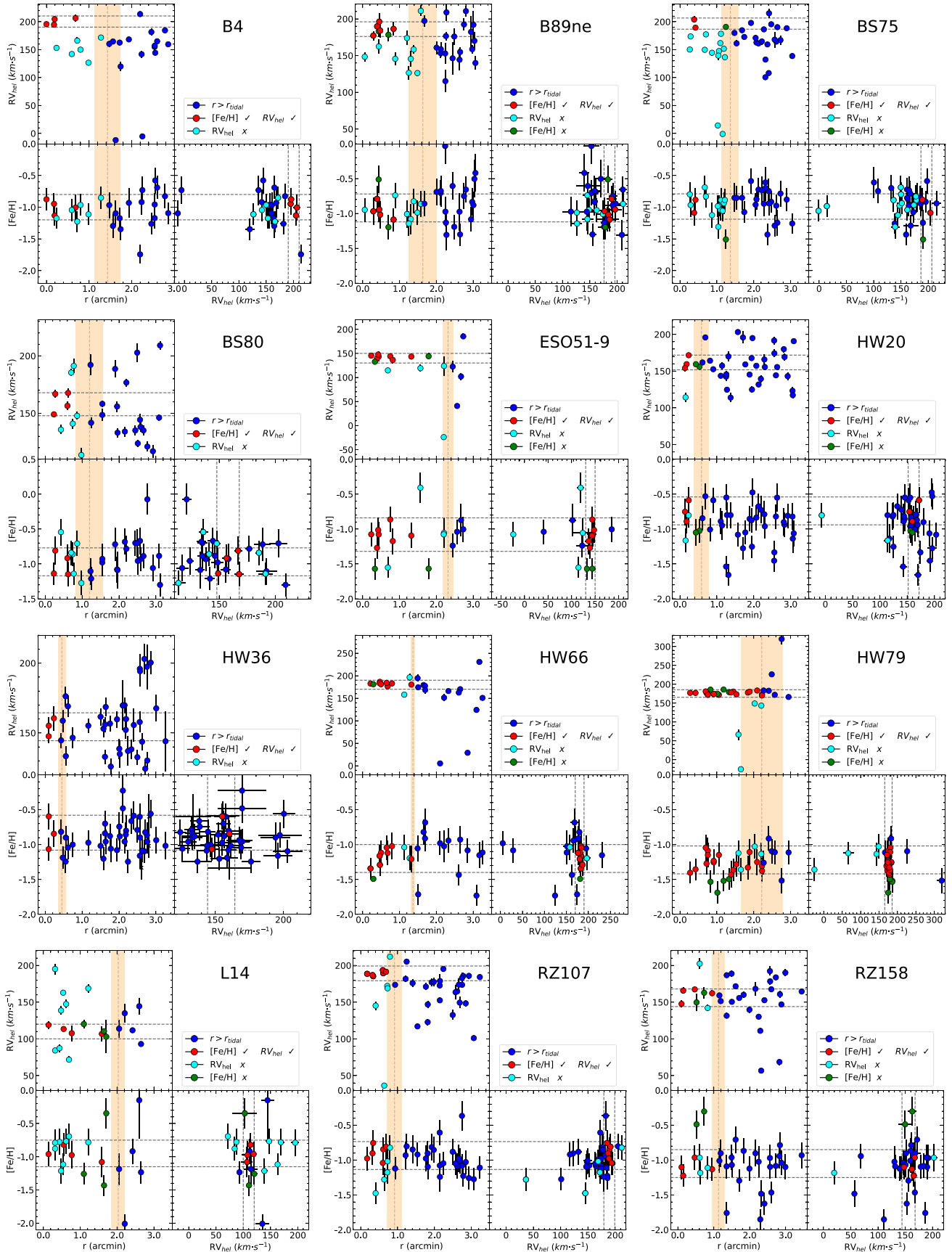


Figure A1. $[\text{Fe}/\text{H}]$, RVs, and distance to the cluster centre of the observed stars. Vertical lines represent our cuts in distance (the corresponding cluster r_t) and horizontal lines our cuts in metallicity and RV.

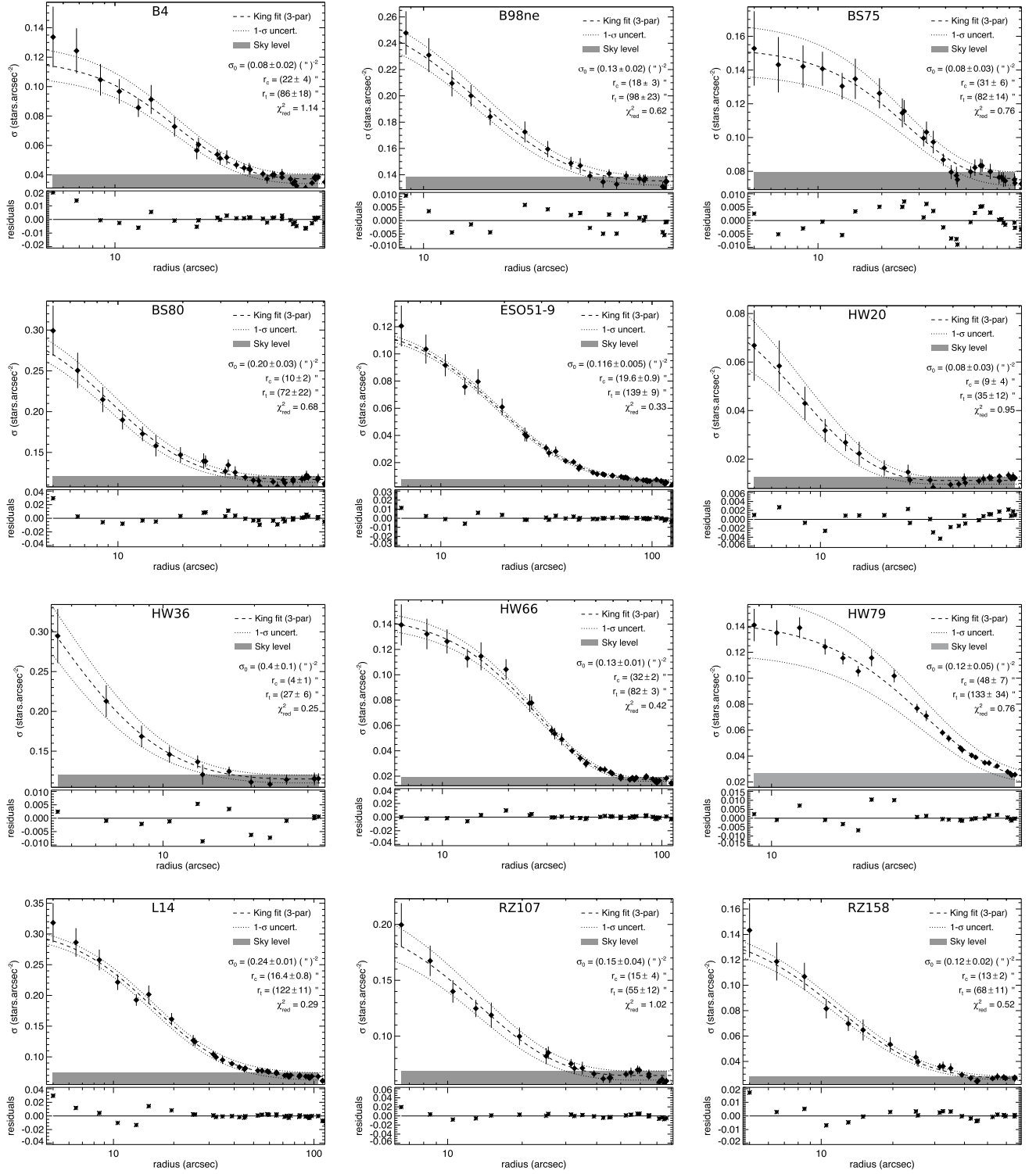


Figure A2. Radial density profiles (diamonds) for clusters of our sample. The fit residuals are shown in the lower sub-panel of each plot.

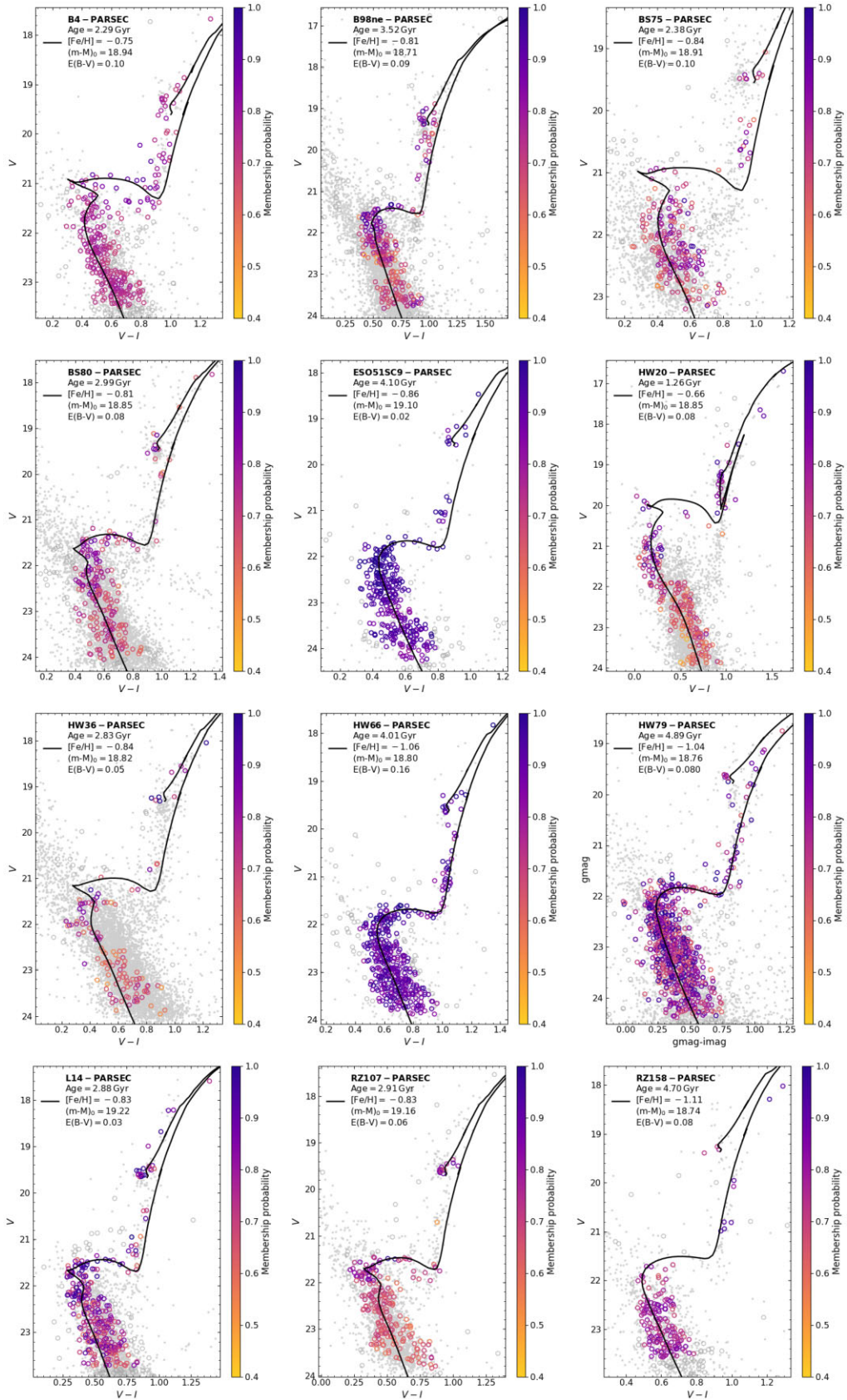


Figure A3. Statistically decontaminated CMDs for our cluster sample. The best-fitting isochrones using the SIRIUS code are shown by the solid lines. Field and probable cluster member stars are represented by grey dots and circles, respectively. The membership probability is identified with the colour code shown in each plot.

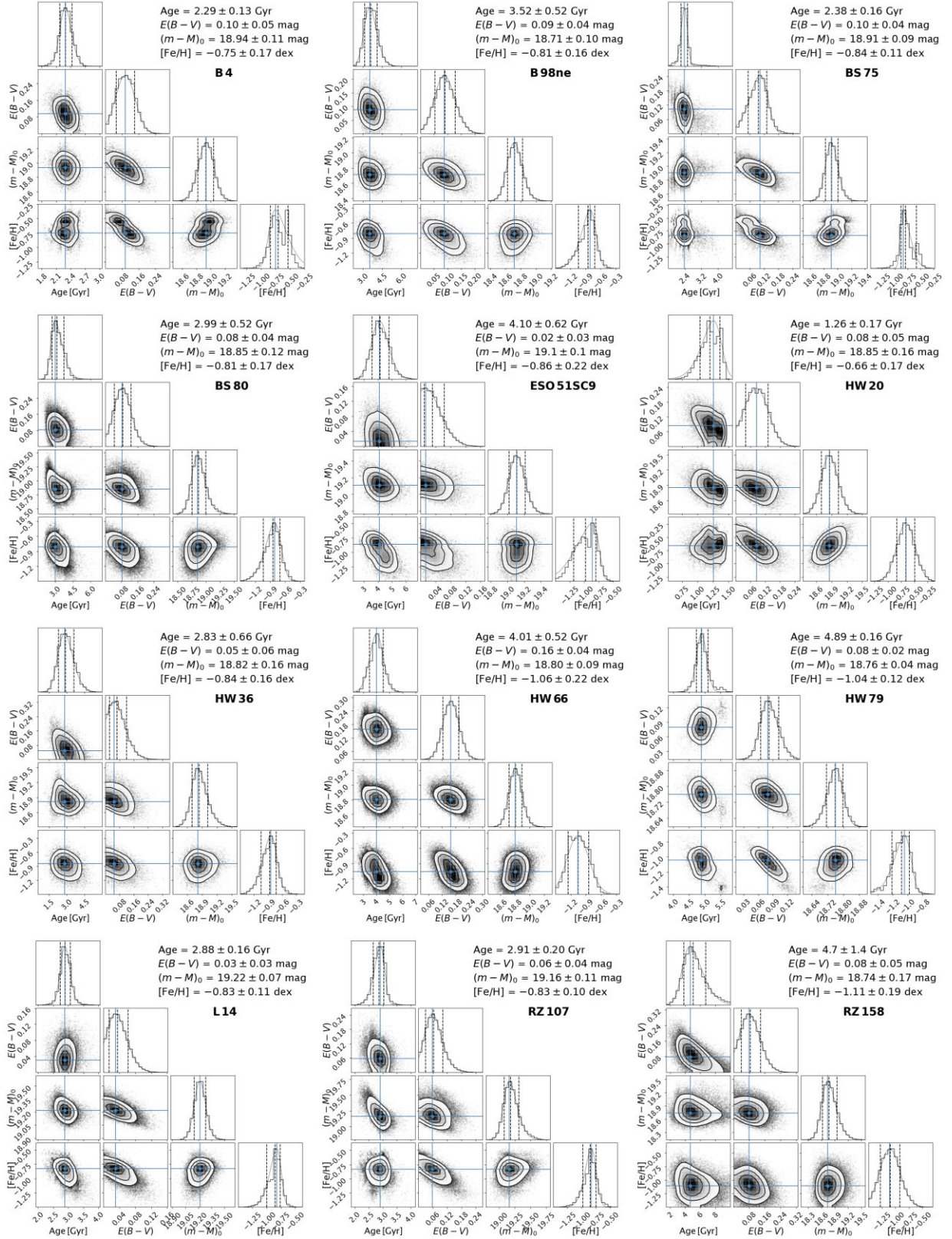


Figure A4. Corner plots for our cluster sample.

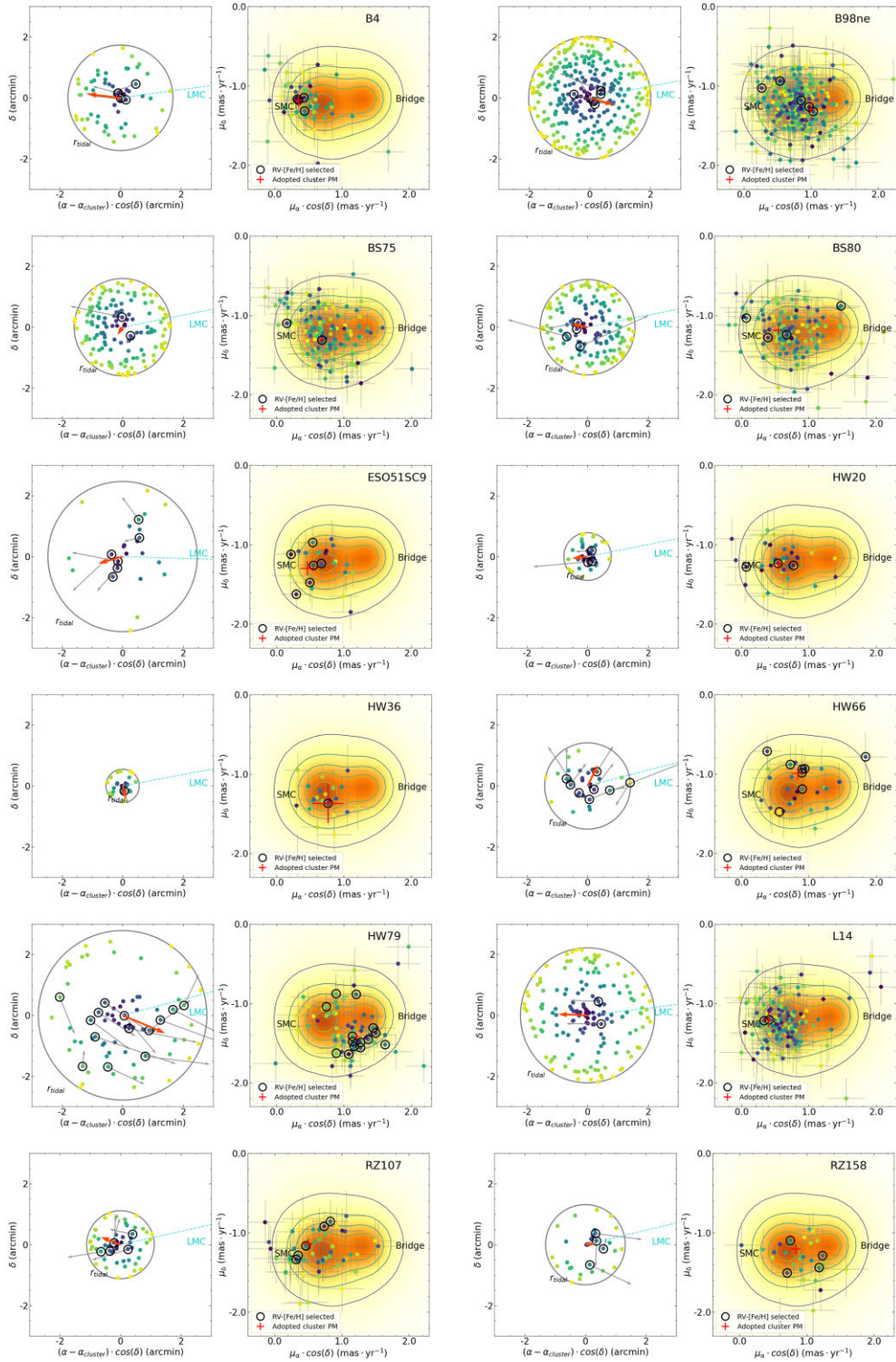


Figure A5. Vector-point diagrams from *Gaia* eDR3 proper motions for the 12 clusters. Left panels: Spatial distributions of *Gaia* stars within the tidal radii of the clusters are shown, with colours indicating the distance from the cluster centre. The spectroscopically selected members are marked with black circles. Grey arrows are *Gaia* eDR3 good-quality proper motions subtracted from the SMC mean proper motion for the spectroscopically selected members, and the red thick arrow is their average PM. The turquoise points towards the LMC. Right panel: The background density plot represents the locus of the SMC and Bridge based on a sample of stars. The points and their error bars are equivalents to the left panels.

This paper has been typeset from a $\text{\TeX}/\text{\LaTeX}$ file prepared by the author.